Chapter 8
Acoustic Excitation for Fluidic Particle Separation

Blake Johnson, Bradon Timms, Jin Yue Trousil, Pavel Vakhlamov, Milo Prisbrey, John Greenhall, and Nicholas Lieven

Abstract During diving operations, eddies generated near sediment beds cause the sediment to mix with water, reducing visibility for divers. Good visibility is critical for applications such as municipal maintenance or coastal construction, where obscured vision can lead to costly delays; naval operations, where turbid water can hamper navigation; and cave diving, where reduced visibility is deadly if the diver cannot locate the cave exit. In this work, we use Ultrasound Separation (UltraSep) as a means of clarifying silt-laden water to improve underwater visibility via a handheld device. The approach uses ultrasonic standing waves that drive particles to coalesce at the standing wave nodes and flocculate, increasing visibility through the rest of the fluid. To determine the effect of UltraSep on fluid clarification, we model the ultrasound, fluid, and hydrodynamic physics in a UltraSep device. Then, we experimentally measured the improvement in visibility and investigated its dependence on excitation power and fluid flow rate. The results from the experimentation with UltraSep not only prove its clarification ability, but also demonstrate that this ability follows a trend—which suggests that this process can be optimized to maximize visibility improvement. The simulations revealed that the acoustic resonance frequency that the chamber should be operated at depends on the initial particle concentration and also changes as the particles move to the nodes and the fluid becomes inhomogeneous. These results suggest the need for implementation of a control system to dynamically adjust the frequency of a device while it operates.

Keywords Ultrasound · separation · filtration · navigation

Blake Johnson
Department of Mechanical and Aerospace Engineering
University of California San Diego, San Diego, CA 92093
e-mail: bjohnson@lanl.gov

Bradon Timms
Department of Mechanical Engineering
Purdue University, West Lafayette, IN 47907
e-mail: timms@lanl.gov

Jin Yue Trousil
Department of Mathematics and Computer Science
Whitworth University, Spokane, WA 99251
e-mail: bjohnson@lanl.gov

Pavel Vakhlamov · Milo Prisbrey · John Greenhall
Los Alamos National Laboratory
Los Alamos New Mexico USA, 87545
e-mail: pvakhlamov@lanl.gov; mprisbrey@lanl.gov; jgreenhall@lanl.gov

Nicholas Lieven
Imperial College London
London SW7 2AZ, UK
e-mail: n.lieven@imperial.ac.uk

© The Author(s), under exclusive license to River Publishers 2026
Kristin B. Zimmerman, PhD (eds.), *Special Topics & Experimental Techniques in Structural Dynamics, 2026, Vol. 5*, Conference Proceedings of the Society for Experimental Mechanics Series, https://doi.org/10.13052/rp-9788743814160

Introduction

Water bed surfaces are often comprised of small particulates, commonly known as silt, that can be easily disturbed and mixed into the surrounding water, reducing visibility through the water (increasing turbidity). This phenomenon can impede or even introduce life-threatening hazards for underwater work such as underwater optical imaging [1], construction [2], inspection [3], and cave diving. For instance, in 2014, the Diver Alert Network reported that visibility was a contributing factor in 31% of diving incidents [4]. There are few existing measures to mitigate this problem. The Divers Alert Network suggests using underwater lights, but cedes that silt-laden water can drastically reduce visibility due to light scattering from the particles. Divers may also use physical lines to help navigate without vision or use strobe lights to mark landmarks. However, these methods do not address the cause of the poor visibility, which is the silt suspended in the water[5]. Low visibility can also increase the time divers take to complete their tasks or potentially force them to surface, both of which lead to increases in cost, required time, and material waste. For object detection, divers may employ handheld tools with magnetic [6] and sonar capabilities [7] to assist them in reduced visibility conditions. However, sonar tools are limited by the strength of the unit and scattering and magnetic tools do not give divers an awareness of their environment and spatial constraints. Thus, there is a critical need for a method of clarifying silt-laden underwater environments by removing particulate. Most existing technologies that can remove particulate or silt rely on filters/membranes or hydrocylones[8]. However, hydrocyclone technology requires high power input causing them to be large and heavy, and filter/membrane systems saturate quickly and require disposable replacements parts.

In this work, we present a method for improving underwater visibility by separating the silt from the water via Ultrasonic Separation (UltraSep). UltraSep utilizes ultrasonic waves to generate Acoustic Radiation Force (ARF) to separate and concentrate particles suspended in a fluid. UltraSep has been adopted in a range of applications including, manipulating and separating individual cells or particles[9], separating cells for flow cytometry[10], focusing powders in laser powder bed fusion additive manufacturing[11], arranging user-specified patterns of microparticles to functionalize structure fabricated via stereolithography[12], and water clarification to remove contaminants[13].

However, acoustic separation techniques are primarily used for biomedical applications currently, as their ability to sort biological samples of relatively uniform size and material from fluids in confined, small (μm-scale) environments non-destructively perfectly suits the needs of the biomedical community[9]. As a result, most research has been focused in this realm with micro-fluidic devices[14]. In contrast, for open underwater activities, the fluid is in an unconstrained body and it can contain particles with a broad range of sizes and material properties. Additionally, existing work does not account for the change in acoustic resonance before steady state as particles move within the bulk medium and create inhomogeneities.

In this work, we demonstrate that UltraSep can be used to improve visibility in silt-laden water, specifically identifying the impact of flow rate and amplitude on the clarification process. In this method, the device pumps water from a larger container through a small acoustic chamber, using the acoustic radiation force from the ultrasonic standing wave to group silt particles so that they coalesce, thus reducing turbidity. We address a real-world application of this technology in the form of a hand-held chamber that can be passed through the water at the will of the diver to clear a region of silt. In addition to the exploring of the the clarification process, we also will simulate the acoustic resonance stability in COMSOL Multiphysics® [15] as the particle concentration changes.

Methods

There are multiple physical phenomena involved in the UltraSep process. The primary acoustic radiation force (ARF), which imparts momentum from the incident wave as it scatters from the particles; secondary radiation force, wherein the scattered wave from each particle scatters again when it interacts with neighboring particles[9]; and viscous drag force, which resists particle motion with respect to the local fluid motion, govern particle movement. In this paper, we excite a flow cell chamber at one of its resonant frequencies to generate a standing ultrasound wave in the cell. Standing waves comprise pressure nodes, where the pressure is zero, and antinodes, where the pressure oscillates periodically between $\pm P_0$, the amplitude of the standing wave. In the standing wave, particles are driven to either the nodes or antinodes based on their density ρ_p and sound speed c_p, in relation to the bulk fluid properties (ρ_f, c_f) [16].

For a particle of radius R in a standing wave with wavelength $\lambda \gg R$, the equation of the time-averaged primary ARF is given as[17]

$$\vec{F} = -\nabla U, \tag{1}$$

where U is the Gor'kov Acoustic Radiation Potential (ARP), given as

$$U = 2\pi R^3 \left[f_{\text{comp}} \frac{1}{3\rho c^2} \overline{p_{in}^2} - f_\rho \frac{\rho}{2} \overline{v_{in}^2} \right]. \tag{2}$$

Here, $\overline{p_{in}^2}$ and $\overline{v_{in}^2}$ are the mean-square fluctuations of the wave pressure and fluid velocity at the particle position. The force amplitude due to pressure and velocity is determined by the coefficients f_{comp} and f_ρ, which are the compressibility and density contrast factors, respectively, and are given as

$$f_{\text{comp}} = 1 - \rho c^2 / \rho_s c_s^2, \text{ and} \tag{3}$$

$$f_\rho = 2(\rho_s - \rho)/(2\rho_s + \rho). \tag{4}$$

We note that in the case of silt particles in water we find $f_{\text{comp}} > 0$ and $f_\rho > 0$, which means that the particles will be driven to the nodes of a standing wave, where $\overline{p_{in}^2} = 0$ and $\overline{v_{in}^2}$ is maximum. For the remainder of this manuscript, we will focus on this scenario, where particles are driven to the nodes.

In addition to ARF, which drives the particles to the nodes, there is drag force $\vec{F}_d$ that resists motion due to ARF and drives the particles with the fluid flow. For small particles at low Reynolds numbers, the drag force is given using Stokes' drag equation[9]

$$\vec{F}_d = -6\mu R\pi \vec{v}. \tag{5}$$

The Stokes drag is influenced by the fluid viscosity μ, the particle radius r_p, and relative velocity between particle and flow v.

In this work, we represent silt separation for an open-channel device both experimentally and with numerical simulations (COMSOL Multiphysics®). The experimental setup is shown in Figure 1.

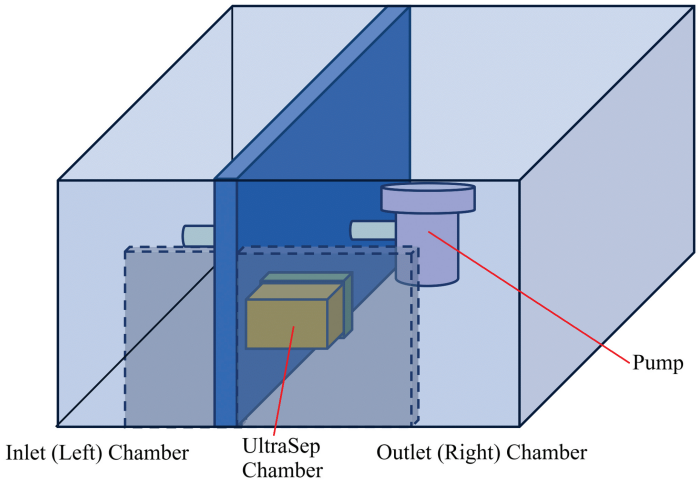

Fig. 1 Depiction of Experimental SetUp

We have represented the motion of the UltraSep silt-separation device through open water by instead pumping water in a tank through the UltraSep device. A tank containing a silt water mixture is separated into two sides. A pump circulates the water from the right side of the tank to the left. The resulting pressure difference forces silt-laden water through the UltraSep device, back to the right side of the tank. From here on, the language in the paper will orient itself to the Ultrasep device—calling the "left side" the "inlet" and "right side" the "outlet". We drive the 17×17×32 mm borosilicate glass UltraSep device with a piezoelectric ultrasonic transducer (PZT-5H, center frequency 2 MHz) to generate vertical standing waves across the device cross section. We investigate the effect of the driving voltage, applied through a power amplifier, on the separation performance. A digital camera is bolted to a fixed position in front of the tank to video the separation process and act as a turbidity sensor.

During each separation experiment, we first turn on the pump to control the flow rate, and agitate both the inlet and outlet sides of the tank to homogenize the suspension of silt. We begin recording video of the flow and then excite the UltraSep transducer. The camera takes a video with a total duration 5 minutes while the system operates to capture the initial flow without separation and steady-state behavior once the silt separation process begins.

To quantify the performance of the UltraSep process, we analyze the water turbidity from the recorded video frames. Two spacial regions of the video frames were inspected: the “inlet region" just before the flow enters the UltraSep device, and the “outlet region" just after the flow exits the UltraSep device,as indicated in Figure 2. By comparing these two regions and their relative turbidities, the performance of the chamber can be assessed.

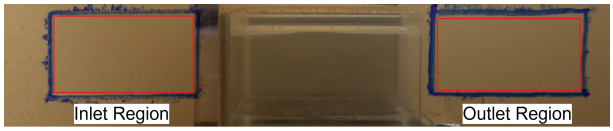

Fig. 2 Depiction of Inlet and Outlet Regions

We implement a turbidity quantification algorithm in MATLAB. The steps of data processing are shown in Figure 3. At each frame of the video, the inlet and outlet regions are isolated and converted to grayscale. We then measure the average pixel value across the inlet frame and across the outlet frame. Repeating this process for each frame in a given experiment results in a vector of turbidity values (average pixel intensities) for both the inlet and outlet regions.

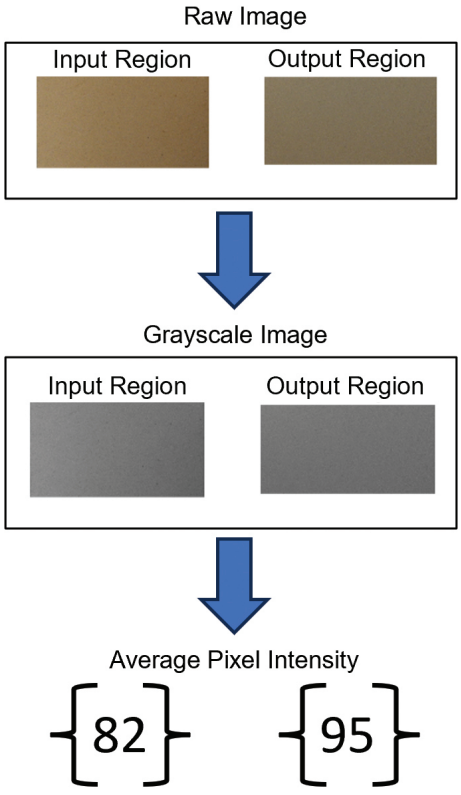

Fig. 3 Depiction of inlet and Output Regions

Due to difference in lighting and background between the inlet and outlet regions and differences in the initial silt dispersal between experiments, we calibrate the inlet and outlet turbidity values. A series of 14 separation experiments were used to determine the absolute minimum and maximum pixel value in both the inlet and outlet. Then for a given experiment the grayscale value of each region was normalized bounded by its respective maximum and minimum. This allowed for comparison of runs with different starting particle concentration, homogeneity, etc.

Additionally, to analyze the results of the experiment properly, the data first needed to be smoothed via a filtering process, so high frequency noise could be removed and clean time derivatives of the trends could be calculated. Data smoothing was

done via the FILTFILT function in MATLAB [18] so there would be no phase change associated with the smoothing; a third-order Butterworth filter was created from the BUTTER function with a normalized cutoff frequency of $0.\overline{333}$ (from a cutoff frequency of 0.05 Hz and sampling frequency of 30 Hz). All difference plots utilize smoothed data, and other plots that utilize smoothed data are labeled as such. Calibration runs to characterize the silt settling without the ultrasonic traducer operating were taken. Three runs of each configuration were tested. The ranges tested were operating the pump at 2.5V and 3V, which corresponds to 6 to 7.4 mL/s. Additionally, the amplitude of the sine wave sent to the box was varied between 100, 150, and 200 mVpp which resulted in true power ranging from 1 to 10 W into the tank.

Trials were made comparable by subtracting the smoothed normalized outlet from the inlet box trend and starting at 0 initial difference. This approach enabled visualization of changes via the relative difference, as in the outlet box became clearer faster than the inlet box. One such plot is given in Figure 4. The average value of the difference was used as the metric to compare runs.

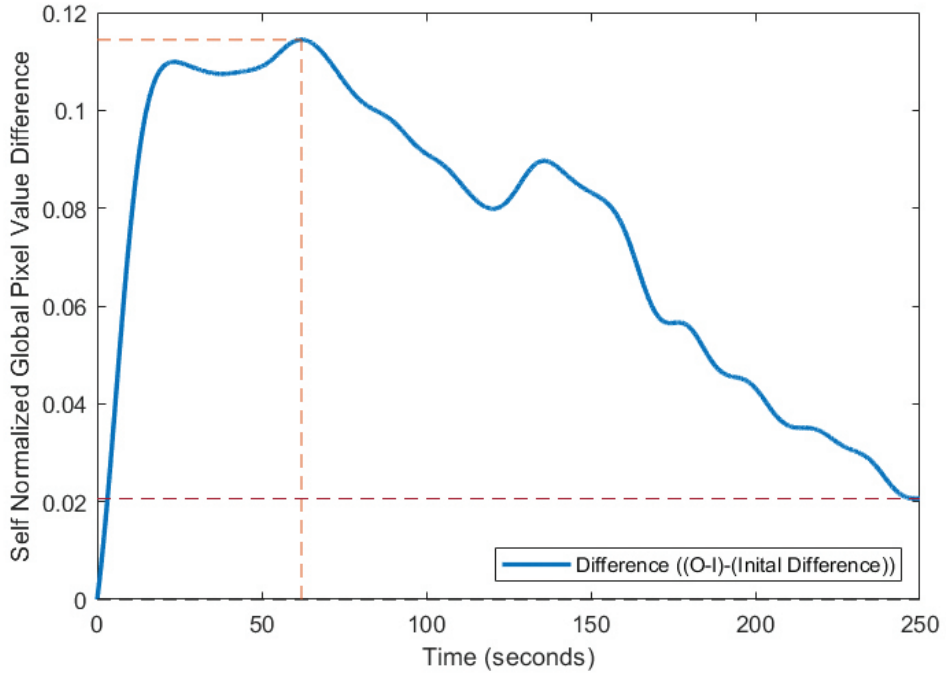

Fig. 4 Inlet Outlet Difference for 6 mL/s flow rate with 3W true power to acoustic chamber

Before each experiment, the same stirring technique was used. The output side of the tank was fully agitated first, then the input side. Once the input side was fully agitated, the output side of the tank was re-agitated for ten more seconds. Then, the whole system was left to settle for ten seconds to avoid high-rate settling of the particulate which would skew the results. The pump was left running during the stirring process to avoid any silt settling in the resonant chamber.

In addition, we retuned the UltraSep excitation frequency in each experiment to ensure that we excited a resonant frequency in the fluid—near the center frequency of the piezoelectric transducer (2 MHz)—to maximize the true power delivered to the UltraSep system. Because of the mismatch in the order of magnitude of the piezoelectric transducer impedance at resonances (single Ω), compared to the output impedance of the power amplifier (50 Ω), we include a 50:3 power transformer between the power amplifier and the transducer. Figure 5 shows an example impedance measurement, consisting of the UltraSep device impedance magnitude (blue) and phase (orange) as a function of frequency. Here, the impedance of the piezoelectric transducer and the fluid resonator are coupled - the gradual trend with minimum at 2 MHz and maximum at approximately 2.1 MHz correspond to the transducer, and the fine peaks spaced approximately every 44 kHz correspond to the fluid resonances. We select the excitation frequency to maximize the true power delivered to the transducer by selecting the fluid resonance near 2 MHz with impedance amplitude as close to 50 Ω ∠0° as possible to match the power amplifier output impedance. In the example shown in 5, we identify 1.96 MHz to be the optimal operating frequency as it corresponds to an impedance of 57.07 Ω ∠0.03°, which was very close to the 50 Ω 0.00° phase impedance needed for perfect impedance matching.

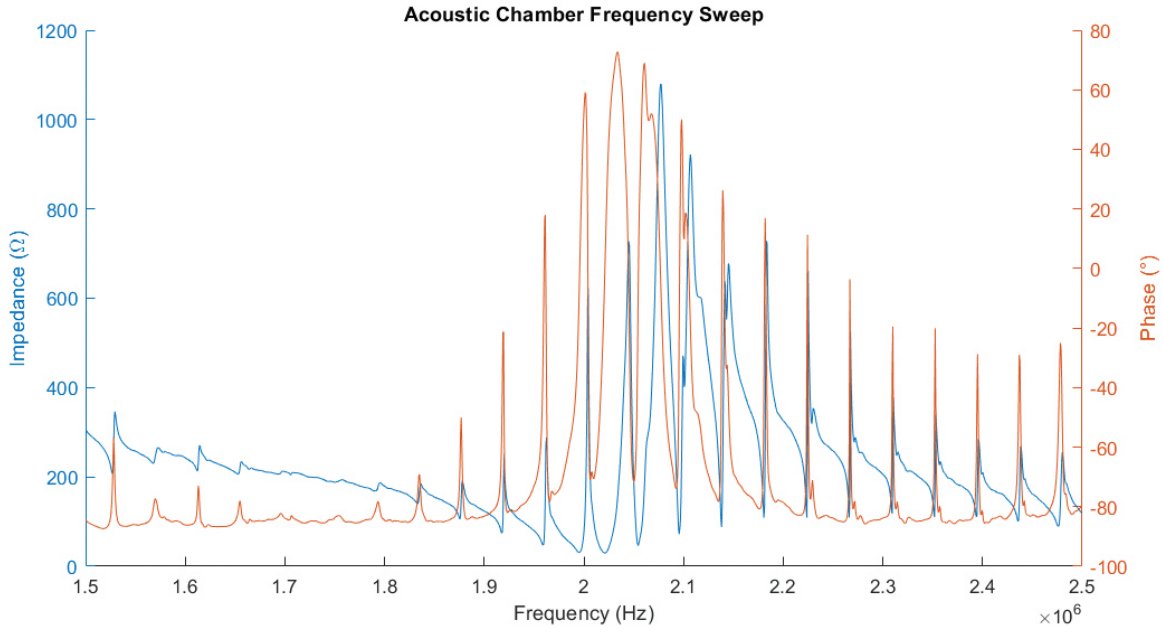

Fig. 5 Impedance measurement of the UltraSep device

Numerical Simulations

Empirically, we observe fluctuations in the resonance frequency during the silt filtration process. This is problematic in practice because when the excitation and resonance frequency differ, the standing wave amplitude drops drastically, reducing the ability to filter the silt. We hypothesize that this is caused by the fluctuating and inhomogeneous density and sound speed in the UltraSep device as the particle distribution changes throughout the separation process. To confirm this hypothesis, we simulate the acoustic field in the UltraSep chamber and the acoustic force on the particles with different particle concentrations. COMSOL Multiphysics® was used to model the acoustic chamber in 2D from a horizontal cross section configuration.

Figure 6 shows the 2D simulation setup. The blue 17mm by 28mm rectangle represents the fluid. The glass walls are represented by two gray 1mm by 28mm rectangles, and the piezoelectric transducer is represented by the brown 1mm by 25mm rectangle. While this figure shows the whole acoustic chamber, in our work, we assumed symmetry across the $y = 14$mm axis to decrease computation time.

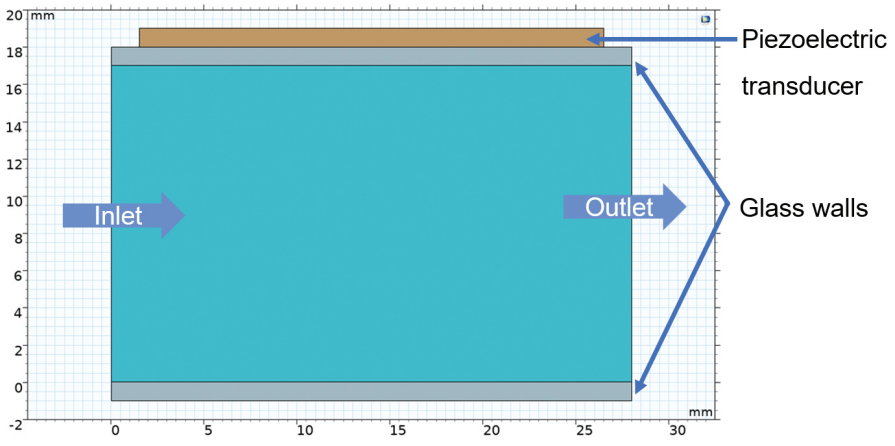

Fig. 6 Model geometry of horizontal cross section view of acoustic chamber

We used COMSOL built-in material properties for the lead zirconate titanate (PZT-5H) transducer, silica glass walls, and water host fluid. For the silt particles, we used the density, $\rho_p = 2690$ kg/m^3, and bulk modulus, $K_p = 3.6 \cdot 10^{10}$ Pa, values from Wang et al. 2018 [19] to calculate the speed of sound, $c_p = \sqrt{\frac{K_p}{\rho_p}} = 3658$m/s. Additionally, the silt particle sizes were measured experimentally using a Microtrac BLUEWAVE particle size analyzer. The distribution of particle sizes can be found in Figure 7. To simplify the ARP computation, we assume a single particle diameter of 5.5μm, the statistical mode of the particle distribution.

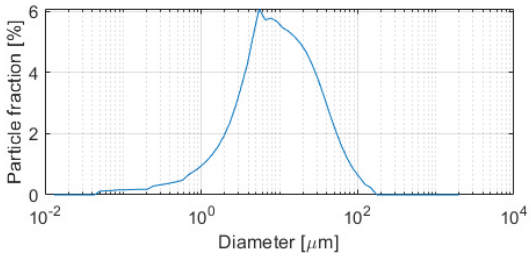

Fig. 7 Particle Size Distribution

The material properties of the bulk medium in the chamber is a function of particle concentration according to rule-of-mixtures formulae,

$$\begin{aligned} c_{eff}(x,y) &= \phi(x,y) \cdot c_p + (1 - \phi(x,y)) \cdot c_f, \text{ and} \\ \rho_{eff}(x,y) &= \phi(x,y) \cdot \rho_p + (1 - \phi(x,y)) \cdot \rho_f. \end{aligned} \tag{6}$$

$\phi(x,y)$ is the spatially varying particle concentration in the acoustic chamber. c_p and c_f are the speed of sound, and ρ_p and ρ_f are the density of the particle and fluid, respectively.

To model the coupled electro-mechanical-acoustic resonance behavior of the system, we used COMSOL's Solid mechanics, Pressure acoustics (frequency domain), and Electrostatics physics modules, as well as the Piezoelectric and Acoustic-structure interface multiphysics modules.

A free quadrilateral mesh was used for the transducer and glass walls, and a mapped mesh was used for the fluid domain. We performed a mesh convergence study, measuring the average von Mises stress in the structural domain, and the average absolute total acoustic pressure in the fluid domain at 2.075MHz.

We decreased the maximum element size of the structural domain from $\frac{1}{2}$(transducer thickness) to $\frac{1}{10}$(transducer thickness). The pressure and stress values computed at each mesh size demonstrate asymptotic convergence as shown in Figure 8. We chose the maximum element size to be $\frac{1}{10}\lambda = 0.1$mm.

We decreased the maximum element size of the structural domain from $\frac{1}{10}\lambda$ to $\frac{1}{19}\lambda$, for $\lambda = \frac{\text{fluid sound speed}}{\text{maximum frequency}}$. In a mesh refinement study, we fitted the values from the code to the model $y* = y(\Delta x) + \beta(\Delta x^p)$, where β is a multiplication constant and p is the rate of convergence. Figure 9 shows the predicted value from the simulation $y(\Delta x)$, the extrapolated solution $y*$ from the model, truncation error $y - y*$, and numerical uncertainty, which is related to the grid convergence index (GCI). In this paper, we used a mesh size of $\frac{1}{14}\lambda = 0.0506803$mm, which results in a GCI of 1.061% and 0.004% for the pressure and stress values respectively.

A frequency sweep study, from 1.9MHz to 2.1, was calculated with uniform particle concentrations of 0%, 1%, 5%, and 10%.

The COMSOL simulation described above can be also be used to solve Equation 7 using COMSOL's Coefficient Form PDE. This results in the particle concentration changing over time in the acoustic field. It is important to note that this method assumes that the resonance frequency and acoustic field are not changing as the particles move to the nodes. However, this serves as an approximation of how the particle distribution changes in a given acoustic field.

Dynamic Density Functional Theory (DDFT) is used to describe the change in particle concentration over time considering entropy $\mu_{ent}(\phi)$, external forces $\mu_{ex}(\phi)$, and interparticle crowding $\mu_{int}(\phi)$ [20]. Entropy describes the random motion of the particles in the fluid. The only external force we consider is the acoustic radiation force. We neglect viscous drag force, as this is a transient force that does not govern the location of the steady state solution. Interparticle crowding imposes a physical constraint on the particle behavior, accounting for particles colliding into each other. The change in particle concentration is described by the partial differential equation,

$$\frac{\partial \phi}{\partial t} = \nabla \cdot [\phi \nabla(\mu_{ent}(\phi) + \mu_{ex}(\phi) + \mu_{int}(\phi))], \tag{7}$$

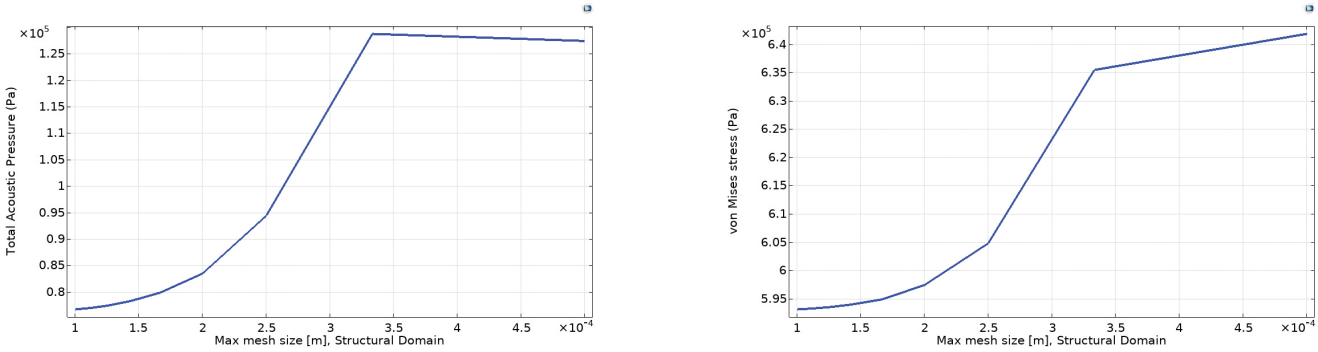

(a) Total acoustic pressure (b) Von Mises stress

Fig. 8 Mesh convergence of the transducer and glass geometries

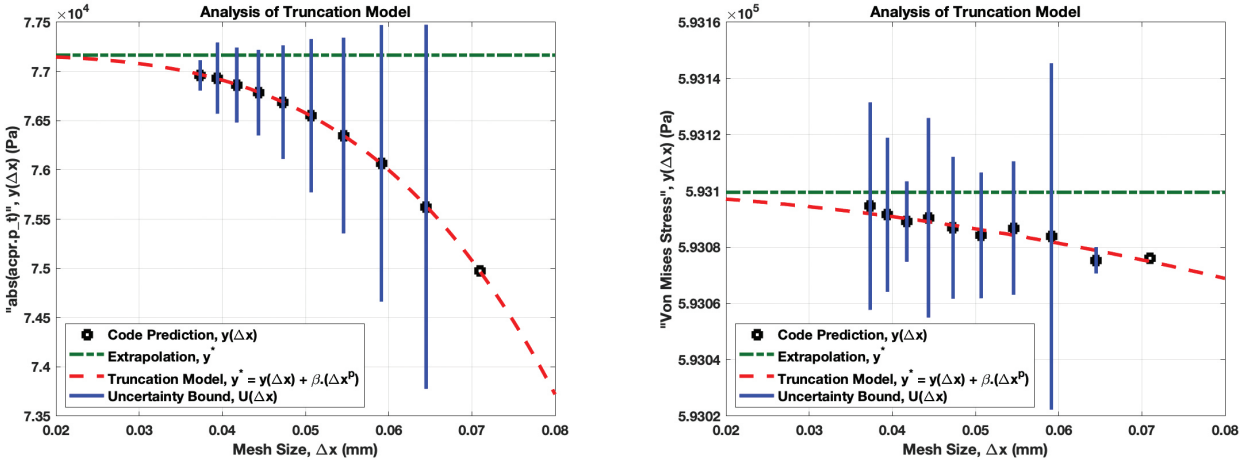

(a) Total acoustic pressure (b) Von Mises stress

Fig. 9 Mesh refinement study of the fluid geometry

where the forcing terms are

$$\begin{aligned} \mu_{ent}(\phi) &= k_B T \ln \phi \\ \mu_{ex}(\phi) &= U \\ \mu_{int}(\phi) &= \frac{1}{(1-\phi)^2}. \end{aligned} \tag{8}$$

Future work in this area can include fine-tuning the time length and step that the solver solves for. Additionally, combining the frequency sweep and PDE studies in the iterative process shown in Figure 10 can give an approximation of how the resonance evolves with the changing particle concentration. In this workflow, given a particle concentration, the effective speed of sound and density in the UltraSep chamber is computed. A frequency sweep is calculated to find the resonance frequency at this particular particle concentration. The acoustic radiation potential (ARP), which governs the movement of the particles, is computed at the resonance frequency using Equation 2. The new distribution of particles is then found by solving Equation 7, as outlined previously. This new distribution of particles is used to find the new effective speed of sound and density. In this way, changes resonance frequency can be measured as the particles are forced to the nodes throughout the UltraSep process.

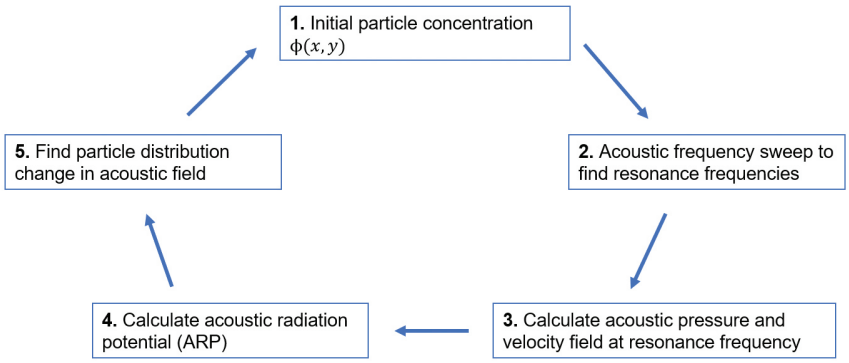

Fig. 10 Iterative process to track resonant behavior throughout UltraSep process

Results

Following the experimental procedure from Methods, we implement the UltraSep experimental method to separate silt from water.

Figure 11 shows the inlet (blue) and outlet (orange) turbidity measurements over time during an experimental and control trial. Both the inlet and outlet regions become less turbid over time, as a direct result of the agitated silt beginning to settle due to gravity. However, across their respective ranges of turbidity, the outlet box much more quickly becomes clearer than the inlet box, which can be attributed to the filtering effect of the acoustic chamber. The control trends mirror one another closely, and both become more clear at around the same rate as gravity settles the silt. Note that the starting conditions do not reflect the efficiency of the clarification and differing starting conditions are addressed by the difference method.

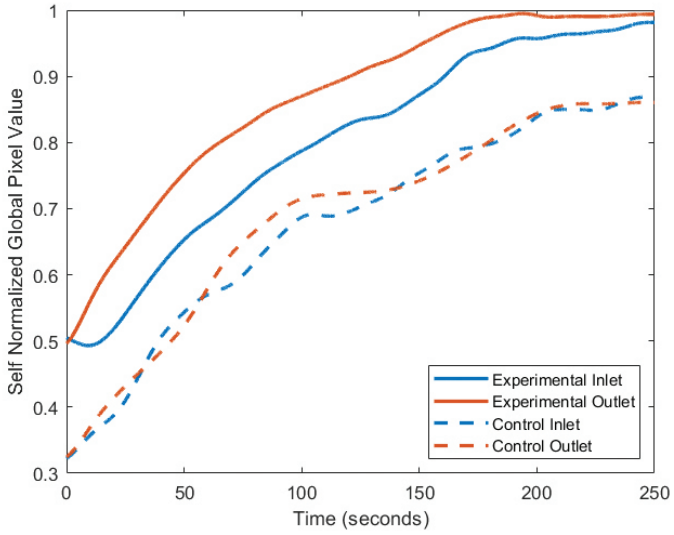

Fig. 11 Smoothed Normalized Inlet and Outlet Trends for 6 mL/s flow rate with 3W true power to acoustic chamber (experimental) and control conditions

In practice, operators will pass the UltraSep device through the water. As a result, it is likely that the device will be required to work for a range of fluid flow rates. At higher flow rates, the particles spend less time within the UltraSep device. Thus, to ensure that they are aggregated while in the device, a stronger acoustic field will be required. To understand how the required power changes with flow rate, we test different combinations of flow rate and true excitation power in the range of 6-7.4 mL/s and 2-10 W, respectively.

Overall, for each flow rate there was an optimal true excitation power, as an inadequate flow rate meant that the particles were trapped by the field, but an excessive flow rate would pull the particles through the chamber before they were trapped

by the acoustic chamber as demonstrated in Figures 12 and 13. For the slower flow rate of 6 mL/s or 2.5V pump there is a moderate negative correlation, which could be attributed to an increasing acoustic field strength preventing trapped particles from flocculating out. However, for the faster flow rate of 7.4 mL/s, better filtration occurs at a higher acoustic field strength. This is likely due to the increasing flow speed requiring a stronger field to force the particles together before they flow out of the chamber. Both of these trends were subjected to a T-test for correlation coefficient and were significant at the 5% significance level. The 6 mL/s flow trend had a t=3.007 and 7.4 mL/s flow trend had a t=3.915 both greater than the critical

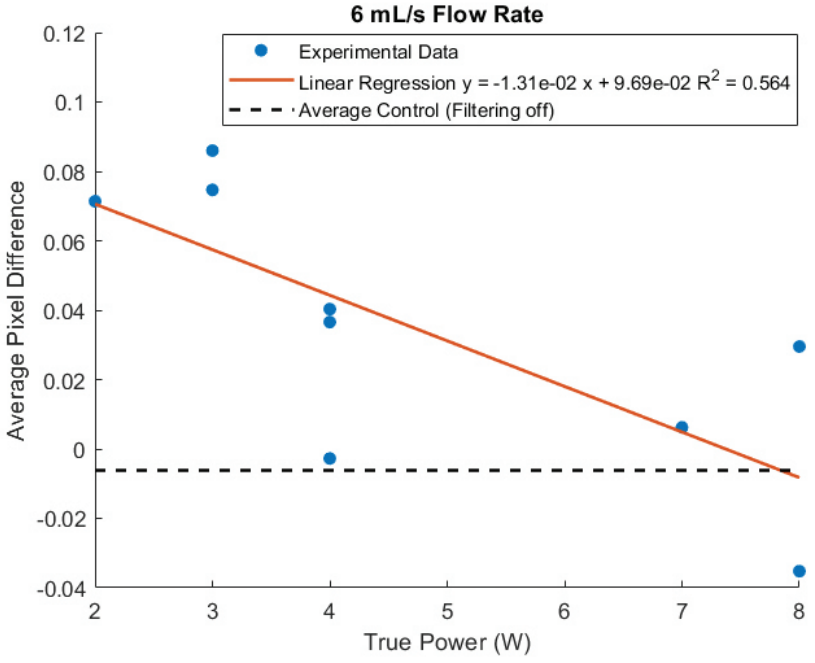

Fig. 12 6 mL/s Flow Rate Trials

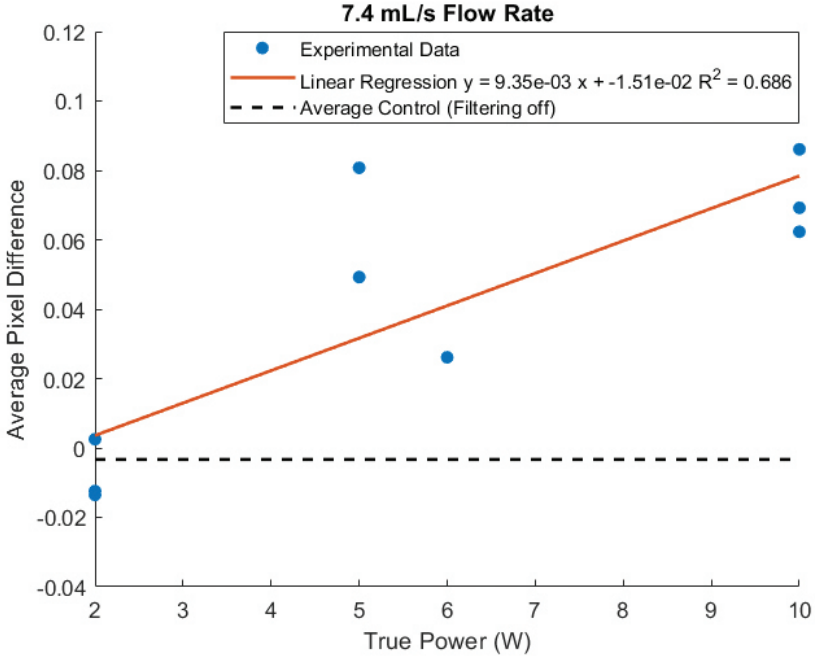

Fig. 13 7.4 mL/s Flow Rate Trials

t value of 2.365. We hypothesize that the variability in data is largely due to inhomogeneous mixing of the tanks as well as the fact that silt above the regions contributed to the amount of light in the inlet and outlet.

The trials were also compared with the excitation voltage to the piezoelectric. For each combination of parameters (flow rate and excitation voltage), a Student T test with $p = 0.05$ ($T_{crit} = 2.92$) was performed against control trials with the UltraSep device unpowered, using the same flow rate. The results are shown in Table 1. At the 5% significance level the 100 mVpp field strength at 6 mL/s and the 200 mVpp at 7.4 mL/s settings filter more effectively than their respective control groups of equal flow rate. This was conducted under the standard assumptions of the T-test.

Table 1 Average Maximum Pixel Difference Experimental Results

Pump Flow Rate (mL/s)	Wave Amplitude (mVpp)	Average Max Pixel Difference	T Value
6	100	0.0773	4.935
6	150	0.0247	1.445
6	200	0.0002	0.2536
7.4	100	-0.0078	-0.2077
7.4	150	0.0520	2.1035
7.4	200	0.0725	3.4200

Critical to the performance of the UltraSep device, however, was operating at a resonance peak. Although an initial frequency sweep was run in free flow conditions with the chamber turned off, once silt began to be captured by the chamber the density of the bulk fluid medium would become inhomogeneous, affecting the location of the resonance.

Following the simulation set up outlined in Methods, we obtained results of the COMSOL simulated frequency sweep with differing uniform particle concentrations. These results are shown in Figure 14. Each line represents a frequency sweep at different uniform particle concentrations of 0%, 1%, 5%, and 10%. Note each line is normalized to the maximum pressure amplitude. As can be seen in Figure 14, the resonance frequencies change with different uniform particle concentrations. This shows that the resonance frequency of the UltraSep device is related to the concentration of particles within the chamber. Further study is needed to investigate how changes in the particle distribution, including nonuniform distributions, impact the resonance frequency.

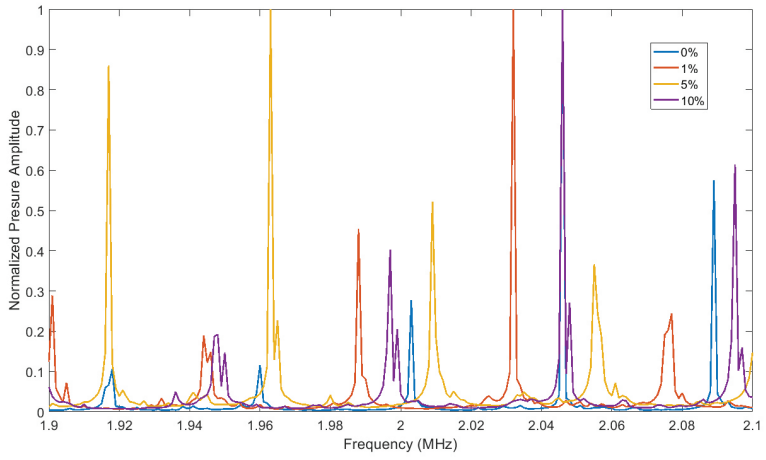

Fig. 14 Frequency sweeps with different uniform particle distributions

Figure 15 shows the initial uniform particle concentration of 5% as it changes in an acoustic field of 1.963MHz. Throughout the timeseries, the concentration of particles at the pressure nodes increases; this reflects the UltraSep process of particles aggregating at the nodes. The separation is most apparent at the midpoint of the chamber, where the standing wave is most stable. The open condition at the edge of the tank and termination of the piezoelectric make the reflection of the acoustic wave more imperfect, therefore the particle aggregation at the nodes is less pronounced.

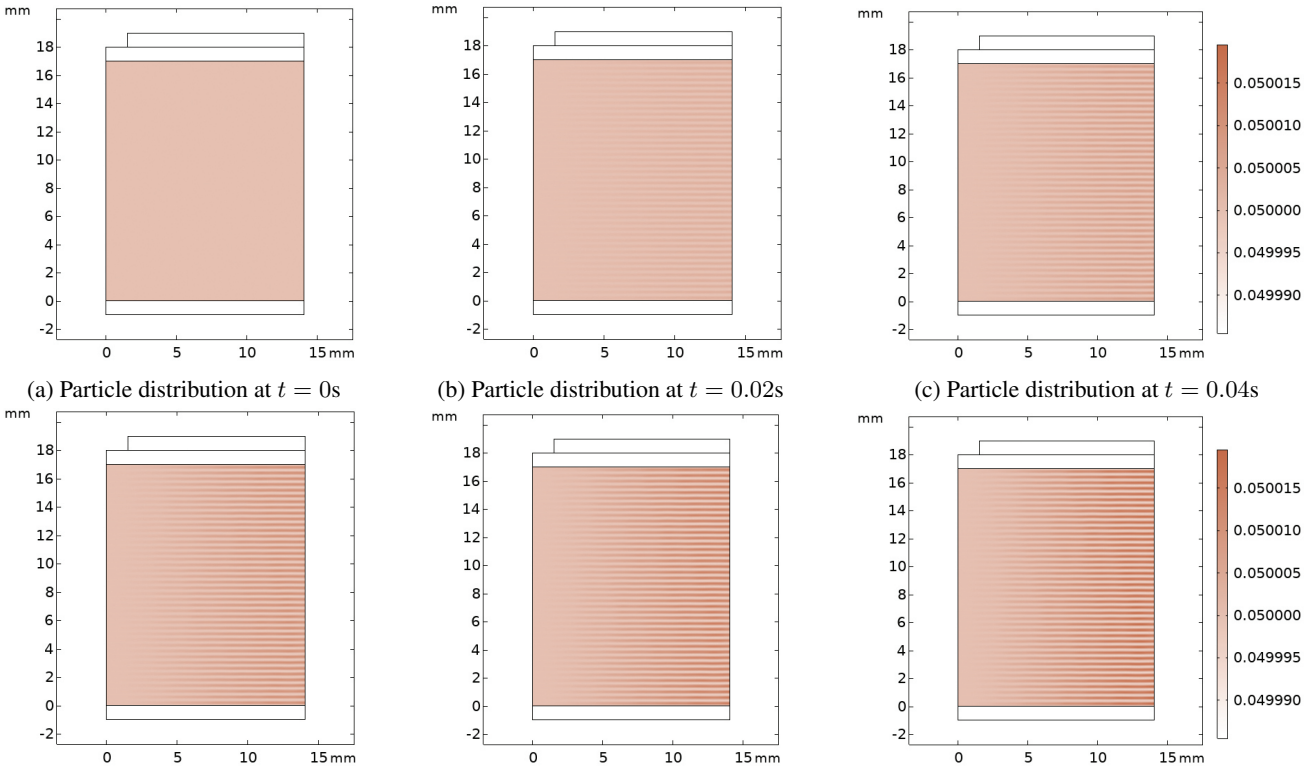

(a) Particle distribution at $t = 0$s (b) Particle distribution at $t = 0.02$s (c) Particle distribution at $t = 0.04$s

(d) Particle distribution at $t = 0.06$s (e) Particle distribution at $t = 0.08$s (f) Particle distribution at $t = 0.1$s

Fig. 15 Particle concentration over time in an acoustic field at 1.963MHz, initial uniform particle concentration of 5%.

Conclusion

Experimentally, we were able to characterize the performance of UltraSep in varying conditions by adjusting flow rate and the strength of the signal delivered to the ultrasonic transducer. The results of the experiments thoroughly demonstrate that UltraSep is a viable technique for fluidic particle separation—relying on flocculation for the clarification of the fluid. The results also suggest that there are points of optimal performance for the process and further work should be done to characterize these optimum points.

Via simulations we demonstrated that the resonant frequency is highly dependent on particle concentrations. This suggests the need for an acoustic filtering device to have a feedback loop that constantly adjusts to where a resonant frequency occurs. Future work would involve an iterative simulation framework, outlined in Methods, where the results of a frequency sweep starting with a constant concentration are used to find where the particles would move, which would generate a new frequency sweep to continue the cycle. In this way patterns in the change in resonance could be uncovered as the distribution of particles changes. However, it has been demonstrated experimentally that even without this control system the acoustic filtration is successfully able to filter the particulate out at a faster rate than gravity alone.

Acknowledgments This research was funded by Los Alamos National Laboratory (LANL) through the Engineering Institute's Los Alamos Dynamics Summer School. The Engineering Institute is a research and education collaboration between LANL and the University of California San Diego's Jacobs School of Engineering. This collaboration seeks to promote multidisciplinary engineering research that develops and integrates advanced predictive modeling, novel sensing systems, and new developments in information technology to address LANL mission-relevant problems. The authors would like to thank Dr. François Hemez, Lawrence Livermore National Laboratory, for his technical advice about the mesh refinement study.

References

1. Wang, Y., Song, W., Fortino, G., Qi, L.Z., Zhang, W., and Liotta, A. "An experimental-based review of image enhancement and image restoration methods for underwater imaging". *IEEE Access*, 7:140233–140251 (2019)ifnextchar.gobble.
2. Alajmi, E. and Alqenaei, A. "Underwater welding techniques". *International Journal of Engineering Research and Applications*, 7(2):14–17 (2017)ifnextchar.gobble.
3. Chemisky, B., Menna, F., Nocerino, E., and Drap, P. "Underwater survey for oil and gas industry: A review of close range optical methods". *Remote Sensing*, 13(14) (2021)ifnextchar.gobble.
4. Penrice, D. and Cooper, J.S. *Diving Casualties*. StatPearls Publishing, Treasure Island (FL) (2025)ifnextchar.gobble.
5. Tillmans, F. "Low-visibility diving - divers alert network" (2022)ifnextchar.gobble.
6. FOSTER, E.J. "A diver-operated underwater metal detector". *Archaeometry*, 12(2):161–166 (1970)ifnextchar.gobble.
7. Schultz, J.J., Healy, C.A., Parker, K., and Lowers, B. "Detecting submerged objects: The application of side scan sonar to forensic contexts". *Forensic Science International*, 231(1):306–316 (2013)ifnextchar.gobble.
8. Kapali, A., Neopane, H., Chitrakar, S., Kayastha, A., and Shrestha, O. "Experimental and cfd study of influence of sediment size on efficiency of hydrocyclone for use as sediment separation device". *Journal of physics. Conference series*, 1608(1):12014 (2020)ifnextchar.gobble.
9. Gao, Y., Wu, M., Lin, Y., and Xu, J. "Acoustic microfluidic separation techniques and bioapplications: A review". *Micromachines*, 11(10) (2020)ifnextchar.gobble.
10. Wu, M., Ozcelik, A., Rufo, J., Wang, Z., Fang, R., and Jun Huang, T. "Acoustofluidic separation of cells and particles". *Microsystems amp; Nanoengineering*, 5(1) (2019)ifnextchar.gobble.
11. Martinez-Marchese, A., Ansari, M., Marzo, A., Wang, M., Soo, S., and Toyserkani, E. "Ultrasound particle lensing: Powder stream control in directed energy deposition using acoustic radiation force fields". *Additive Manufacturing*, 73:103698 (2023)ifnextchar.gobble.
12. Greenhall, J. and Raeymaekers, B. "3d printing macroscale engineered materials using ultrasound directed self-assembly and stereolithography". *Advanced Materials Technologies*, 2(9):1700122 (2017)ifnextchar.gobble.
13. Hawkes, J.J., Coakley, W.T., Gröschl, M., Benes, E., Armstrong, S., Tasker, P.J., and Nowotny, H. "Single half-wavelength ultrasonic particle filter: Predictions of the transfer matrix multilayer resonator model and experimental filtration results". *The Journal of the Acoustical Society of America*, 111(3):1259–1266 (2002)ifnextchar.gobble.
14. Drinkwater, B.W. "Dynamic-field devices for the ultrasonic manipulation of microparticles". *Lab Chip*, 16:2360–2375 (2016)ifnextchar.gobble.
15. "Comsol multiphysics® v. 6.3. www.comsol.com. comsol ab, stockholm, sweden.".
16. Zhang, Y. and Chen, X. "Particle separation in microfluidics using different modal ultrasonic standing waves". *Ultrasonics Sonochemistry*, 75:105603 (2021)ifnextchar.gobble.
17. Barmatz, M. and Collas, P. "Acoustic radiation potential on a sphere in plane, cylindrical, and spherical standing wave fields". *The Journal of the Acoustical Society of America*, 77(3):928–945 (1985)ifnextchar.gobble.
18. Inc., T.M. "Matlab version: 24.2.0.2806996 (r2024b update 3)" (2024)ifnextchar.gobble.
19. Wang, J., Liu, B., Kan, G., Li, G., Zheng, J., and Meng, X. "Frequency dependence of sound speed and attenuation in fine-grained sediments from 25 to 250 khz based on a probe method". *Ocean Engineering*, 160:45–53 (2018)ifnextchar.gobble.
20. Rauscher, M. *Dynamic Density Functional Theory (DDFT)*, pages 1–8. Springer US, Boston, MA (2013)ifnextchar.gobble.